

Article

Computational Approach to Dynamic Systems through Similarity Measure and Homotopy Analysis Method for Renewable Energy

Noor Saeed Khan ^{1,2,3,*} , Poom Kumam ^{1,2,4,*}  and Phatiphat Thounthong ⁵ 

- ¹ KMUTT Fixed Point Research Laboratory, Room SCL 802 Fixed Point Laboratory, Science Laboratory Building, Department of Mathematics, Faculty of Science, King Mongkut's University of Technology Thonburi (KMUTT), Bangkok 10140, Thailand
 - ² Center of Excellence in Theoretical and Computational Science (TaCS-CoE), Science Laboratory Building, Faculty of Science, King Mongkut's University of Technology Thonburi (KMUTT), 126 Pracha-Uthit Road, Bang Mod, Thung Khru, Bangkok 10140, Thailand
 - ³ Department of Mathematics, Division of Science and Technology, University of Education, Lahore 54000, Pakistan
 - ⁴ Department of Medical Research, China Medical University Hospital, China Medical University, Taichung 40402, Taiwan
 - ⁵ Renewable Energy Research Centre, Department of Teacher Training in Electrical Engineering, Faculty of Technical Education, King Mongkut's University of Technology North Bangkok, 1518 Pracharat 1 Road, Wongsawang, Bangsue, Bangkok 10800, Thailand; phatiphat.t@ieee.org
- * Correspondence: noor.saeed@ue.edu.pk (N.S.K.); poom.kum@kmutt.ac.th (P.K.)

Received: 6 October 2020; Accepted: 10 November 2020; Published: 27 November 2020



Abstract: To achieve considerably high thermal conductivity, hybrid nanofluids are some of the best alternatives that can be considered as renewable energy resources and as replacements for the traditional ways of heat transfer through fluids. The subject of the present work is to probe the heat and mass transfer flow of an ethylene glycol based hybrid nanofluid (Au-ZnO/C₂H₆O₂) in three dimensions with homogeneous-heterogeneous chemical reactions and the nanoparticle shape factor. The applications of appropriate similarity transformations are done to make the corresponding non-dimensional equations, which are used in the analytic computation through the homotopy analysis method (HAM). Graphical representations are shown for the behaviors of the parameters and profiles. The hybrid nanofluid (Au-ZnO/C₂H₆O₂) has a great influence on the flow, temperature, and cubic autocatalysis chemical reactions. The axial velocity and the heat transfer increase and the concentration of the cubic autocatalytic chemical reactions decreases with increasing stretching parameters. The tangential velocity and the concentration of cubic autocatalytic chemical reactions decrease and the heat transfer increases with increasing Reynolds number. A close agreement of the present work with the published study is achieved.

Keywords: Au-ZnO/C₂H₆O₂; heat transfer; rotating systems; analytical solution

1. Introduction

Energy has a crucial role in the prosperity and development of any country. The daily consumed energy resources like natural gas, oil, and coal are certain to vanish with the passage of time because these are huge sources of energy and are being depleted due to their limited availability. To cope with such a situation, the replenishment of the world's energy is of utmost concern, making it a basic requirement to search for some reliable and affordable energy alternatives. Such problems apply to renewable energy systems. Nanoparticles have been shown to solve such constraints because

of their remarkable heat transfer capabilities. The application of nanoparticles in the industrial, biomedical, and energy sectors is due to their thermophysical properties. Nanoparticles have seen applications in energy conversion (e.g., fuel cells, solar cells, and thermoelectric devices), energy storage (e.g., rechargeable batteries and super capacitors), and energy saving (e.g., insulation such as aerogels and smart glazes, efficient lightning like light emitting diodes and organic light-emitting diodes). To combat climate change, clean and sustainable energy sources need to be rapidly developed. Solar energy technology converts solar energy directly into electricity, for which high performance cooling, heating, and electricity generation are among the inevitable requirements. In solar collectors, the absorbed incident solar radiation is converted to heat. The working fluid conveys the generated heat for different uses [1]. Etefaghi et al. [2] worked on a bio-nanoemulsion fuel based on biodegradable nanoparticles to improve diesel engines' performance and reduce exhaust emissions. Gunjo et al. [3] investigated the melting enhancement of a latent heat storage with dispersed Cu, CuO, and Al₂O₃ nanoparticles for a solar thermal application. Khanafer and Vafai [4] presented a review on the applications of nanofluids in the solar energy field.

Nanofluids reduce the process time, enhance the heating rates, and improve the lifespan of machinery [5]. Nanofluids have seen applications in power saving, manufacturing, transportation, healthcare, microfluidics, nano-technology, microelectronics, etc. Recently, nano-technology has attracted great attraction from scientists [6]. Nanoparticles are the most interesting technology to introduce novel, environmentally friendly chemical and mechanical polishing slurries to fabricate effective materials [7]. Thermal conductivity is of great importance and is enhanced by the incorporation of nanoparticles in the base fluid [8]. Hamilton and Crosser [9] studied the thermal conductivity of a heterogeneous two component system. Nanofluids were obtained by the addition of nanoparticles to the base fluids, and they have gained popularity since the work of Choi and Eastman [10]. Vallejo et al. [11] analyzed the internal aspects of the fluid for six carbon-based nanomaterials in a rotating rheometer with a double conic shape containing a typical sheet. Alihosseini and Jafari [12] investigated a three-dimensional computational fluid dynamics model for an aluminum foam and nanoparticles with heat transfer using a number of cylinders having different configurations through a permeable medium. Sheikholeslami et al. [13], working with a ethylene glycol nanofluid, discussed the electric field, thermal radiation, and nanoparticle shape factors of a ferrofluid by showing that the platelet shape led to enhanced convective flow. Al-Kouz et al. [14] applied computational fluid dynamics to analyze entropy generation in a rarefied time dependent, laminar two-dimensional flow of an air-aluminum oxide nanofluid in a cavity with a square shape having more than one solid fin at the heated wall where the optimization procedure was adopted to show the conditions by which the overall entropy generation was reduced. Atta et al. [15] modified the asphaltenes isolated from crude oil to work as capping agents for the synthesis of hydrophobic silica to investigate the surface charge of hydrophobic silica nanoparticles, the chemical structure, the particle size, and the surface morphology. Rout et al. [16] presented the three and higher order nonlinear thin film study and optics fabricated with gold nanoparticles. They obtained the solution via spin-coating techniques to achieve the highest values of nonlinear absorption coefficient, nonlinear refractive index and saturation intensity. Alvarez-Regueiro et al. [17] experimentally determined the heat transfer coefficients and pressure drops of four functionalized graphene nanoplatelet nanofluids for heat transfer enhancement to discuss the nanoadditive loading, temperature and Reynolds number. Alsagri et al. [18] elaborated the heat and mass transfer flow of single walled and multi walled carbon nanotubes past a stretchable cylinder by investigating that the heat transfer enhances with the high values of nanoparticles concentration of single walled carbon nanotubes compared to that of multi walled carbon nanotubes. Working on transverse vibration, Mishra et al. [19] comparatively investigated a computational fluid dynamic model for water based nanofluid through a pipe subject to superimposed vibration, applied to the wall to increase the heat transfer in axial direction while vibration effect is decreased for pure liquid and is increased for nanofluid. Abbas et al. [20] achieved the results that in the heat and mass transfer flow of

Cross nanofluid, the Bejan number was intensified for the high values of thermal radiation parameter. Some discussion on nanofluids and other relevant studies can be found in the references [21–55].

Mono-nanofluids represent enhanced thermal conductivity and good rheological characteristics, but still they have some weak characteristics necessary for a particular purpose. By the hybridization process, different nanoparticles are added in a base fluid to make the hybrid nanofluid which has enhanced thermophysical properties and thermal conductivity as well as rheological properties. Ahmad et al. [56] investigated the hybrid nanofluid with activation energy and binary chemical reaction through a moving wedge taken into account the Darcy law of porous medium, heat generation, thermal slip, radiation, and variable viscosity. Dinarvand and Rostami [57] presented the ZnO-Au hybrid nanofluid when 15 gm of nanoparticles are added into the 100 gm base fluid, the heat transfer enhances more than 40% compared to that of the regular fluid.

Homogeneous-heterogeneous chemical reactions have important applications in chemical industries. Ahmad and Xu [58] worked on homogeneous-heterogeneous chemical reactions in which the reactive species were of regular size reacting with other species in a nanofluid to show more realistic mathematical model physically. Hayat et al. [59] elaborated the Xue nanofluid model to study the carbon nanotubes nanofluids in rotating systems incorporating Darcy–Forchheimer law, homogeneous-heterogeneous chemical reactions and optimal series solutions. Suleman et al. [60] addressed the homogeneous-heterogeneous chemical reactions in Ag-H₂O nanofluid flow past a stretching sheet with Newtonian heating to prove that concentration field was decreased for the increasing strength of homogeneous-heterogeneous chemical reactions.

In the literature, interesting studies exist like [5] which investigates the electrical conductivity, structural and optical properties of ZnO. In study [6], the theoretical and experimental results of electric current and thermal conductivity of H₂O-ethylene glycol based TiO₂ have been obtained. The study [7] relates to the oxide-ethylene glycol nanofluid with different sizes of nanoparticles. Due to the applications of the above studies, it is desired to investigate the ethylene glycol based Au-ZnO hybrid nanofluid flow with heat transfer and homogeneous-heterogeneous chemical reactions in rotating system. The present study has the applications in renewable energy technology, thermal power generating system, spin coating, turbo machinery etc. The solution of the problem is obtained through an effective technique known as homotopy analysis method [61]. Investigations are shown through graphs and discussed in detail.

2. Methods

A rotating flow of hydromagnetic, time independent and incompressible hybrid nanofluid between two parallel disks in three dimensions is analyzed. Homogeneous-heterogeneous chemical reactions are also considered. The lower disk is supposed to locate at $z = 0$ while the upper disk is at a constant distance H apart. The velocities and stretching on these disks are (Ω_1, Ω_2) and (a_1, a_2) , respectively while the temperatures on these disks are T_1 and T_2 , respectively. A magnetic field of strength B_0 is applied in the direction of z -axis (please see Figure 1). Ethylene glycol is chosen for the base fluid in which zinc oxide and gold nanoparticles are added.

For cubic auto-catalysis, the homogeneous reaction is



The first order isothermal reaction on the surface of catalyst is



where B and C denote the chemical species with concentrations b and c , respectively. k_c and k_s are the rate constants.

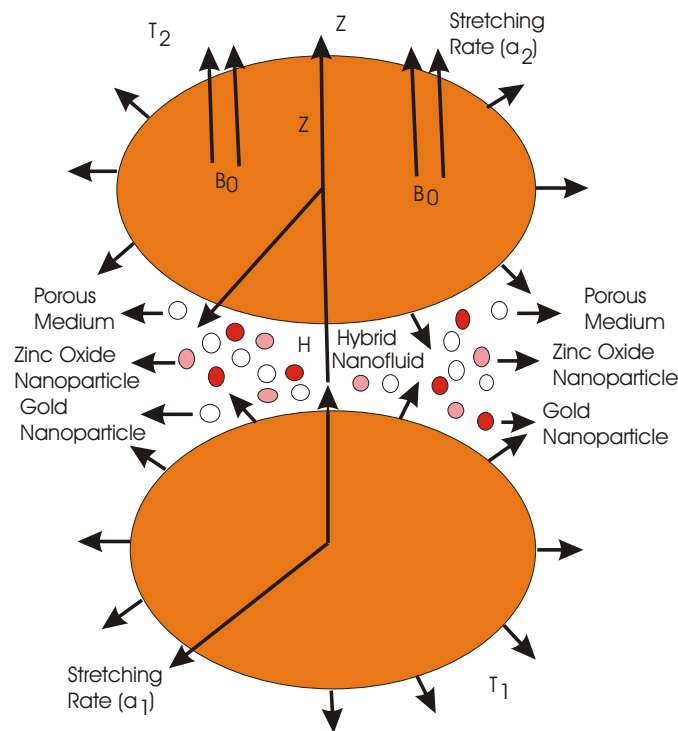


Figure 1. Geometry of the problem.

Cylindrical coordinates (r, θ, z) , are applied to provide the thermodynamics of hybrid nanofluid as [57–59]

$$\frac{\partial w}{\partial z} + \frac{\partial u}{\partial r} + \frac{u}{r} = 0, \tag{3}$$

$$\rho_{hnf} \left(-\frac{v^2}{r} + \frac{\partial u}{\partial r} u + \frac{\partial u}{\partial z} w \right) = \mu_{hnf} \left(\frac{\partial^2 u}{\partial z^2} + \frac{\partial^2 u}{\partial r^2} - \frac{u}{r^2} + \frac{\partial u}{\partial r} \frac{1}{r} \right) - \sigma_{hnf} B_0^2 u - \frac{\mu_{hnf}}{S} u^2 - S_1 u^2 - \frac{\partial P}{\partial r}, \tag{4}$$

$$\rho_{hnf} \left(\frac{uv}{r} + w \frac{\partial v}{\partial z} + u \frac{\partial v}{\partial r} \right) = \mu_{hnf} \left(\frac{\partial^2 v}{\partial z^2} + \frac{\partial^2 v}{\partial r^2} - \frac{v}{r^2} + \frac{1}{r} \frac{\partial v}{\partial r} \right) - \sigma_{hnf} B_0^2 v - \frac{\mu_{hnf}}{S} v^2 - S_1 v^2, \tag{5}$$

$$\rho_{hnf} \left(w \frac{\partial w}{\partial z} + u \frac{\partial w}{\partial r} \right) = -\frac{\partial P}{\partial z} + \mu_{hnf} \left(\frac{\partial^2 w}{\partial z^2} + \frac{\partial^2 w}{\partial r^2} + \frac{1}{r} \frac{\partial w}{\partial r} \right) - \frac{\mu_{hnf}}{S} w^2 - S_1 w^2, \tag{6}$$

$$(\rho c_p)_{hnf} \left(w \frac{\partial T}{\partial z} + u \frac{\partial T}{\partial r} \right) = \left(k_{hnf} + \frac{16T_1^3 \sigma_1}{3k_0} \right) \left(\frac{\partial^2 T}{\partial z^2} + \frac{\partial^2 T}{\partial r^2} + \frac{1}{r} \frac{\partial T}{\partial r} \right) + \sigma_{hnf} B_0^2 (v^2 + u^2), \tag{7}$$

$$w \frac{\partial b}{\partial z} + u \frac{\partial b}{\partial r} = -c^2 b k_c + D_B \left(\frac{\partial^2 b}{\partial z^2} + \frac{\partial^2 b}{\partial r^2} + \frac{1}{r} \frac{\partial b}{\partial r} \right), \tag{8}$$

$$w \frac{\partial c}{\partial z} + u \frac{\partial c}{\partial r} = c^2 b k_c + D_C \left(\frac{\partial^2 c}{\partial z^2} + \frac{\partial^2 c}{\partial r^2} + \frac{1}{r} \frac{\partial c}{\partial r} \right). \tag{9}$$

The boundary conditions are

$$\text{at } z = 0, \quad D_C \frac{\partial c}{\partial z} = k_s c, \quad D_B \frac{\partial b}{\partial z} = k_s b, \quad T = T_1, \quad w = 0, \quad v = r\Omega_1, \quad u = ra_1, \tag{10}$$

$$\text{at } z = H, \quad c \rightarrow 0, \quad b \rightarrow b_0, \quad T = T_2, \quad P \rightarrow \infty, \quad w = 0, \quad v = r\Omega_2, \quad u = ra_2, \tag{11}$$

where $u(r, \theta, z)$, $v(r, \theta, z)$ and $w(r, \theta, z)$ are the components of velocity, P is the pressure. S is the permeability of porous medium, $S_1 = \frac{C_b}{rS^2}$ is the non-uniform inertia coefficient of porous medium with C_b as the drag coefficient. Temperature of hybrid nanofluid is T and $B = (0, 0, B_0)$ is the magnetic field. σ_1 is the Stefan Boltzmann constant and k_0 is the absorption coefficient. For the hybrid nanofluid, the important quantities are ρ_{hnf} (density), μ_{hnf} (dynamic viscosity), σ_{hnf} (electrical conductivity), $(c_p)_{hnf}$ (heat capacity) and k_{hnf} (thermal conductivity). The subscript “hnf” shows

the hybrid nanofluid. For the thermal conductivity, the mathematical formulation is obtained via Hamilton–Crosser model [9] as

$$\frac{k_{nf}}{k_f} = \frac{k_1 + (n_1 - 1)k_f - (n_1 - 1)(k_f - k_1)\phi_1}{k_1 + (n_1 - 1)k_f + (k_f - k_1)\phi_1}, \quad (12)$$

where n is the empirical shape factor for the nanoparticle whose value is given in Table 1.

Table 1. Values of shape factor of different shapes of nanoparticles.

Shapes of Nanoparticle	n	Aspect Ratio
Spherical	3	-
Brick	3.7	1:1:1
Cylinder	4.8	1:8
Platelet	5.7	1:1/8

The subscript “ f ” denotes the base fluid namely ethylene glycol and the subscript “ nf ” is used for nanofluid. ρ_s and $(c_p)_s$ are the density and heat capacity at specified pressure of nanoparticles, respectively. ϕ_1 is the first nanoparticle volume fraction while ϕ_2 is the second nanoparticle volume fraction which can be formulated as [57].

$$\rho_s = \frac{(\rho_1 \times m_1) + (\rho_2 \times m_2)}{m_1 + m_2}, \quad (13)$$

$$(c_p)_s = \frac{((c_p)_1 \times m_1) + ((c_p)_2 \times m_2)}{m_1 + m_2}, \quad (14)$$

$$\phi_1 = \frac{\frac{m_1}{\rho_1}}{\frac{m_1}{\rho_1} + \frac{m_2}{\rho_2} + \frac{m_f}{\rho_f}}, \quad (15)$$

$$\phi_2 = \frac{\frac{m_2}{\rho_2}}{\frac{m_1}{\rho_1} + \frac{m_2}{\rho_2} + \frac{m_f}{\rho_f}}, \quad (16)$$

$$\phi = \phi_1 + \phi_2, \quad (17)$$

where m_1 , m_2 and m_f are, respectively the mass of first nanoparticle, mass of the second nanoparticle and mass of the base fluid. ϕ is the total volume fraction of zinc oxide and gold nanoparticles.

The thermophysical properties of $C_2H_6O_2$ as well as nanoparticles are given in Table 2.

Table 2. Thermophysical properties of ethylene glycol and nanoparticles.

Properties	Ethylene Glycol ($C_2H_6O_2$)	Zinc Oxide (ZnO)	Gold (Au)
ρ (kg/m ³)	$\rho_f = 116.6$	$\rho_{s_1} = 5600$	$\rho_{s_2} = 19,282$
c_p (J/kg K)	$(c_p)_f = 2382$	$(c_p)_{s_1} = 495.2$	$(c_p)_{s_2} = 192$
k (W/m K)	$k_f = 0.249$	$k_{s_1} = 13$	$k_{s_2} = 310$
σ (Um) ⁻¹	$\sigma_f = 3.14$	$\sigma_{s_1} = 7.261 \times 10^{-9}$	$\sigma_{s_2} = 4.11 \times 10^7$
Nanoparticle measurement/nm	-	29 and 77	3–40

The mathematical formulations for ρ_{hnf} (density), μ_{hnf} (dynamic viscosity), σ_{hnf} (electrical conductivity), $(c_p)_{hnf}$ (heat capacity) are given in Table 3 where ϕ_s shows the particle concentration.

Table 3. Mathematical forms of thermophysical properties.

Properties	ZnO/C ₂ H ₆ O ₂
Density (ρ)	$\rho_{nf} = (1 - \phi_1)\rho_f + \phi_1\rho_s$
Heat capacity (ρc_p)	$(\rho c_p)_{nf} = (1 - \phi_1)(\rho c_p)_f + \phi_1(\rho c_p)_s$
Dynamic viscosity (μ)	$\frac{\mu_{nf}}{\mu_f} = \frac{1}{(1 - \phi_1)^{2.5}}$
Thermal conductivity (k)	$\frac{k_{nf}}{k_f} = \frac{k_1 + (n_1 - 1)k_f - (n_1 - 1)(k_f - k_1)\phi_1}{k_1 + (n_1 - 1)k_f + (k_f - k_1)\phi_1}$
Electrical conductivity (σ)	$\frac{\sigma_{nf}}{\sigma_f} = 1 + \frac{3(\sigma - 1)\phi_1}{(\sigma + 2) - (\sigma - 1)\phi_1}$, where $\sigma = \frac{\sigma_s}{\sigma_f}$
Properties	Hybrid nanofluid (Au-ZnO/C ₂ H ₆ O ₂)
Density (ρ)	$\rho_{hnf} = (1 - (\phi_1 + \phi_2))\rho_f + \phi_1\rho_{s_1} + \phi_2\rho_{s_2}$
Heat capacity (ρc_p)	$(\rho c_p)_{hnf} = (1 - (\phi_1 + \phi_2))(\rho c_p)_f + \phi_1(\rho c_p)_{s_1} + \phi_2(\rho c_p)_{s_2}$
Dynamic viscosity (μ)	$\frac{\mu_{hnf}}{\mu_f} = \frac{1}{[1 - (\phi_1 + \phi_2)]^{2.5}}$
Thermal conductivity (k)	$\frac{k_{hnf}}{k_f} = \frac{k_2 + (n_2 - 1)k_{nf} - (n_2 - 1)(k_{nf} - k_2)\phi_2}{k_2 + (n_2 - 1)k_{nf} + (k_{nf} - k_2)\phi_2} \times \frac{k_1 + (n_1 - 1)k_f - (n_1 - 1)(k_f - k_1)\phi_1}{k_1 + (n_1 - 1)k_f + (k_f - k_1)\phi_1} \times k_f$
Electrical conductivity (σ_{hnf})	$\frac{\sigma_{hnf}}{\sigma_f} = 1 + \frac{3 \left[\frac{\sigma_1\phi_1 + \sigma_2\phi_2}{\sigma_f} - (\phi_1 + \phi_2) \right]}{2 + \left[\frac{\sigma_1\phi_1 + \sigma_2\phi_2}{(\phi_1 + \phi_2)\sigma_f} \right] - \left[\frac{\sigma_1\phi_1 + \sigma_2\phi_2}{\sigma_f} - (\phi_1 + \phi_2) \right]}$

Following transformations are used

$$f'(\zeta)\Omega_1 r = u, \quad v = r\Omega_1 g(\zeta), \quad -2f(\zeta)H\Omega_1 = w, \quad \frac{-T_2 + T}{-T_2 + T_1} = \theta(\zeta), \quad \Omega_1 \rho_f \nu_f \left(\frac{\epsilon r^2}{2H^2} + P(\zeta) \right) = P, \\ \varphi b_0 = b, \quad c = b_0 \varphi_1, \quad \frac{z}{H} = \zeta, \quad (18)$$

where $\nu_f = \frac{\mu_f}{\rho_f}$ is the kinematic viscosity and ϵ is the pressure parameter.

Using the values from Equation (18) in Equations (4)–(11), the following eight Equations (19)–(26) are obtained

$$B_1 f''' + Re \left(2ff'' - f'^2 + g^2 - MB_2 f' \right) - \epsilon - k_2 Re B_1 f' - k_3 Re \frac{1}{\rho_{hnf}} (f')^2 = 0, \quad (19)$$

$$B_1 g'' + Re \left(2fg' - MB_2 g' \right) - k_2 Re B_1 g - k_3 Re \frac{1}{\rho_{hnf}} (g)^2 = 0, \quad (20)$$

$$P' = \frac{2}{k_2} - 4Reff' - f', \quad (21)$$

$$B_3 \frac{k_{hnf}}{k_f} \theta'' + \frac{1}{Ra} Pr Re \left[2f\theta' + MEcB_4 \left(g^2 + (f')^2 \right) \right] = 0, \quad (22)$$

$$Sc Re \left(2\varphi'f - k_4 \varphi \varphi_1^2 \right) + \varphi'' = 0, \quad (23)$$

$$\varphi_1'' + Sc Re \left(2\varphi_1'f + k_4 \varphi \varphi_1^2 \right) \frac{1}{k_5} = 0, \quad (24)$$

$$f = 0, \quad f' = k_6, \quad g = 1, \quad \theta = 1, \quad \varphi' = k_7 \varphi, \quad k_4 \varphi_1' = -k_7 \varphi, \quad P = 0 \quad \text{at} \quad \zeta = 0, \quad (25)$$

$$f = 0, \quad f' = k_8, \quad g = \Omega, \quad \theta = 0, \quad \varphi = 1, \quad \varphi_1 = 0 \quad \text{at} \quad \zeta = 1, \quad (26)$$

where (') represents the derivative with respect to ζ . $B_1 = \left[1 - \frac{\frac{m_1}{\rho_1}}{\frac{m_1}{\rho_1} + \frac{m_2}{\rho_2} + \frac{m_f}{\rho_f}} \right]^{-2.5}$
 $\times \left[1 - \frac{\frac{m_1}{\rho_1}}{\frac{m_1}{\rho_1} + \frac{m_2}{\rho_2} + \frac{m_f}{\rho_f}} + \frac{\frac{m_1}{\rho_1}}{\frac{m_1}{\rho_1} + \frac{m_2}{\rho_2} + \frac{m_f}{\rho_f}} \frac{\rho_s}{\rho_f} \right]^{-1}$, $B_2 = 1 + \frac{3 \left[\frac{\sigma_1 \phi_1 + \sigma_2 \phi_2}{\sigma_f} - (\phi_1 + \phi_2) \right]}{2 + \left[\frac{\sigma_1 \phi_1 + \sigma_2 \phi_2}{(\phi_1 + \phi_2) \sigma_f} \right] - \left[\frac{\sigma_1 \phi_1 + \sigma_2 \phi_2}{\sigma_f} - (\phi_1 + \phi_2) \right]}$,
 $B_3 = \frac{(\rho c_p)_f}{\left[\left[1 - \frac{\frac{m_1}{\rho_1}}{\frac{m_1}{\rho_1} + \frac{m_2}{\rho_2} + \frac{m_f}{\rho_f}} \right] \rho_f + \left[1 - \frac{\frac{m_1}{\rho_1}}{\frac{m_1}{\rho_1} + \frac{m_2}{\rho_2} + \frac{m_f}{\rho_f}} \right] \rho_s \right] \times \left[\left[1 - \frac{\frac{m_1}{\rho_1}}{\frac{m_1}{\rho_1} + \frac{m_2}{\rho_2} + \frac{m_f}{\rho_f}} \right] (C_p)_f + \left[1 - \frac{\frac{m_1}{\rho_1}}{\frac{m_1}{\rho_1} + \frac{m_2}{\rho_2} + \frac{m_f}{\rho_f}} \right] (C_p)_s \right]}$,
 $B_4 = \frac{\sigma_{lmf}}{\rho_{lmf}}$. $k_2 = \frac{\nu_f}{S \Omega_1}$ is the porosity parameter, $k_3 = \frac{C_b}{S^2}$ is the inertial parameter due to Darcy Forchheimer effect. The other non-dimensional parameters are $\Omega = \frac{\Omega_2}{\Omega_1}$, $Re = \frac{\Omega_1 H^2}{\nu_f}$, $M = \frac{\sigma_f B_0^2}{\rho_f \Omega_1}$, $Rd = \frac{16 \sigma_1 T_1^3}{3 k_f k_0}$, $Pr = \frac{(\rho c_p)_{lmf} \nu_f}{k_f}$,
 $Ec = \frac{r^2 \Omega_1^2}{c_p (T_1 - T_2)}$, $Sc = \frac{\nu_f}{D_B}$, $k_4 = \frac{k_c b_0^2}{\Omega_1}$, $k_5 = \frac{D_C}{D_B}$, $k_6 = \frac{a_1}{\Omega_1}$, $k_7 = \frac{k_s H}{D_B}$ and $k_8 = \frac{a_2}{\Omega_1}$ which are known as rotation parameter, Reynolds number, magnetic field parameter, thermal radiation parameter, Prandtl number, Eckert number, Schmidt number, homogeneous chemical reaction parameter, diffusion coefficient ratio, stretching parameter for lower disks, heterogeneous chemical reaction parameter and stretching parameter at upper disk, respectively.

Regarding the homogeneous-heterogeneous chemical reaction, the quantities B and C may be considered in a special case, i.e., if D_B is equal to D_C , then in such a case k_5 equals unity, which leads to

$$1 = \varphi_1(\zeta) + \varphi(\zeta). \tag{27}$$

Using Equation (27), Equations (23) and (24) generate

$$0 = ScRe \left[(1 - \varphi)^2 k_4 \varphi + 2\varphi' f \right] + \varphi'', \tag{28}$$

whose corresponding boundary conditions become

$$\varphi' = k_7 \varphi \text{ for } \zeta = 0 \text{ while } \varphi = 1 \text{ for } \zeta = 1. \tag{29}$$

By taking derivative of Equation (19) with respect to ζ , it becomes

$$B_1 f'''' + Re \left(2ff'' + 2gg' - MB_2 f' \right) - k_2 Re B_1 f'' - 2k_3 Re \frac{1}{\rho_{lmf}} f f'' = 0. \tag{30}$$

Considering Equation (21), Equations (25) and (26), the quantity ϵ is computed as

$$\epsilon = f'''(0) - Re \left[- (g(0))^2 + (f'(0))^2 + MB_2 f'(0) + \frac{1}{B_1 k_2 f'(0)} \right]. \tag{31}$$

Integrating Equation (21) with respect to ζ by using the limit 0 to ζ for evaluating P as

$$P = -2 \left[Re \left((f)^2 + \frac{1}{k_2} \int_0^\zeta f \right) (f' - f'(0)) \right]. \tag{32}$$

Skin Frictions and Nusselt Numbers

The important physical quantities are defined as

$$C_{f_1} (\text{Local skin friction at lower disk}) = \frac{\tau|_{z=0}}{\rho_{lmf} (r \Omega_1)^2},$$

$$C_{f_2} (\text{Local skin friction at upper disk}) = \frac{\tau|_{z=H}}{\rho_{lmf} (r \Omega_1)^2}, \tag{33}$$

where

$$\tau = \sqrt{(\tau_{zr})^2 + (\tau_{z\theta})^2}, \tag{34}$$

denotes the sum of shear stress of tangential forces τ_{zr} and $\tau_{z\theta}$ along radial and tangential directions which are defined as

$$\begin{aligned} \tau_{zr} \text{ (Shear stress friction at lower disk)} &= \mu_{hnf} \frac{\partial u}{\partial z} \Big|_{z=0} = \frac{\mu_{hnf} r \Omega_1 f''(0)}{H} \text{ and} \\ \tau_{z\theta} &= \mu_{hnf} \frac{\partial v}{\partial z} \Big|_{z=0} = \frac{\mu_{hnf} r \Omega_1 g'(0)}{H}. \end{aligned} \tag{35}$$

Using the information of Equations (34) and (35), Equation (33) proceeds to

$$C_{f_1} = \frac{1}{Re_r} \left[1 - \frac{\frac{m_1}{\rho_1}}{\frac{m_1}{\rho_1} + \frac{m_2}{\rho_2} + \frac{m_f}{\rho_f}} \right]^{-2.5} \left[(f''(0))^2 + (g'(0))^2 \right]^{\frac{1}{2}}, \tag{36}$$

$$C_{f_2} = \frac{1}{Re_r} \left[1 - \frac{\frac{m_1}{\rho_1}}{\frac{m_1}{\rho_1} + \frac{m_2}{\rho_2} + \frac{m_f}{\rho_f}} \right]^{-2.5} \left[(f''(1))^2 + (g'(1))^2 \right]^{\frac{1}{2}}, \tag{37}$$

where $Re_r = \frac{r\Omega_1 H}{\nu_{hnf}}$ is the Reynolds number.

Another important physical quantity is

$$\begin{aligned} Nu_{r_1} \text{ (Local Nusselt number at lower disk)} &= \frac{Hq_w}{k_f(T_1 - T_2)} \Big|_{z=0}, \\ Nu_{r_2} \text{ (Local Nusselt number at upper disk)} &= \frac{Hq_w}{k_f(T_1 - T_2)} \Big|_{z=H}, \end{aligned} \tag{38}$$

where q_w is the surface temperature defined as

$$q_w \text{ (At lower disk)} = -k_{hnf} \frac{\partial T}{\partial z} \Big|_{z=0} = -k_{hnf} \frac{T_1 - T_2}{H} \theta'(0). \tag{39}$$

Taking information from Equation (39), Equation (38) becomes

$$Nu_{r_1} = -\frac{k_{hnf}}{k_f} \theta'(0), \quad Nu_{r_2} = -\frac{k_{hnf}}{k_f} \theta'(1). \tag{40}$$

3. Computational Methodology

Following the HAM, choosing the initial guesses and linear operators for the velocities, temperature and homogeneous-heterogeneous chemical concentration profiles as

$$\begin{aligned} f_0(\zeta) &= \zeta^3(k_6 + k_8) - \zeta^2(2k_6 + k_8) + \zeta k_6, \quad g_0(\zeta) = \zeta\Omega + 1 - \zeta, \quad \theta_0(\zeta) = -\zeta + 1, \\ \varphi_0(\zeta) &= \frac{\zeta k_7 + 1}{k_7 + 1}, \end{aligned} \tag{41}$$

$$\varphi'' = L_\varphi, \quad f'''' = L_f, \quad g'' = L_g, \quad \theta'' = L_\theta, \tag{42}$$

characterizing

$$L_f [E_1 + E_2\zeta + E_3\zeta^2 + E_4\zeta^3] = 0, \quad L_g [E_5 + E_6\zeta] = 0, \quad L_\theta [E_7 + E_8\zeta] = 0, \quad L_\varphi [E_9 + E_{10}\zeta] = 0, \tag{43}$$

where $E_i(i = 1-10)$ are the arbitrary constants.

3.1. Zeroth Order Deformation Problems

Introducing the nonlinear operator \aleph as

$$\aleph_f[f(\zeta, j), g(\zeta, j)] = B_1 \frac{\partial^4 f(\zeta, j)}{\partial \zeta^4} + Re \left[2f(\zeta, j) \frac{\partial^3 f(\zeta, j)}{\partial \zeta^3} + 2g(\zeta, j) \frac{\partial g(\zeta, j)}{\partial \zeta} - MB_2 \frac{\partial^2 f(\zeta, j)}{\partial \zeta^2} \right] - k_2 Re B_1 \frac{\partial^2 f(\zeta, j)}{\partial \zeta^2} - 2k_3 Re \frac{1}{\rho_{lmf}} \frac{\partial f(\zeta, j)}{\partial \zeta} \frac{\partial^2 f(\zeta, j)}{\partial \zeta^2}, \quad (44)$$

$$\aleph_g[f(\zeta, j), g(\zeta, j)] = B_1 \frac{\partial^2 g(\zeta, j)}{\partial \zeta^2} + Re \left[2f(\zeta, j) \frac{\partial g(\zeta, j)}{\partial \zeta} - MB_2 \frac{\partial g(\zeta, j)}{\partial \zeta} \right] - k_2 B_1 g(\zeta, j) - k_3 \frac{1}{\rho_{lmf}} [g(\zeta, j)]^2, \quad (45)$$

$$\aleph_\theta[f(\zeta, j), g(\zeta, j), \theta(\zeta, j)] = B_3 \frac{k_{lmf}}{k_f} \frac{\partial^2 \theta(\zeta, j)}{\partial \zeta^2} + \frac{1}{Rd} Pr Re \left[2f(\zeta, j) \frac{\partial \theta(\zeta, j)}{\partial \zeta} + MB_4 Ec \left(\frac{\partial f(\zeta, j)}{\partial \zeta} \right)^2 + (g(\zeta, j))^2 \right], \quad (46)$$

$$\aleph_\varphi[f(\zeta, j), \varphi(\zeta, j)] = \frac{\partial^2 \varphi(\zeta, j)}{\partial \zeta^2} + Re Sc \left[2f(\zeta, j) \frac{\partial \varphi(\zeta, j)}{\partial \zeta} + k_4 \varphi(\zeta, j) (1 - \varphi(\zeta, j))^2 \right], \quad (47)$$

where j is the homotopy parameter such that $j \in [0, 1]$.

Moreover

$$(1 - j)L_f[f(\zeta, j) - f_0(\zeta)] = j\hbar_f \aleph_f[f(\zeta, j), g(\zeta, j)], \quad (48)$$

$$(1 - j)L_g[g(\zeta, j) - g_0(\zeta)] = j\hbar_g \aleph_g[f(\zeta, j), g(\zeta, j)], \quad (49)$$

$$(1 - j)L_\theta[\theta(\zeta, j) - \theta_0(\zeta)] = j\hbar_\theta \aleph_\theta[f(\zeta, j), g(\zeta, j), \theta(\zeta, j)], \quad (50)$$

$$(1 - j)L_\varphi[\varphi(\zeta, j) - \varphi_0(\zeta)] = j\hbar_\varphi \aleph_\varphi[f(\zeta, j), \varphi(\zeta, j)], \quad (51)$$

where $\hbar_\varphi, \hbar_f, \hbar_\theta$ and \hbar_g are the convergence control parameters.

Boundary conditions of Equation (48) are

$$f(0, j) = 0, \quad f'(0, j) = k_6, \quad f(1, j) = 0, \quad f'(1, j) = k_8. \quad (52)$$

Boundary conditions of Equation (49) are

$$g(0, j) = 1, \quad g(1, j) = \Omega. \quad (53)$$

Boundary conditions of Equation (50) are

$$\theta(0, j) = 1, \quad \theta(1, j) = 0. \quad (54)$$

Boundary conditions of Equation (51) are

$$\varphi'(0, j) = k_7 \varphi(0, j), \quad \varphi(1, j) = 1. \quad (55)$$

Characterizing $j = 0$ and $j = 1$, the calculations obtained as

$$j = 0 \Rightarrow f(\zeta, 0) = f_0(\zeta) \quad \text{and} \quad j = 1 \Rightarrow f(\zeta, 1) = f(\zeta), \quad (56)$$

$$j = 0 \Rightarrow g(\zeta, 0) = g_0(\zeta) \quad \text{and} \quad j = 1 \Rightarrow g(\zeta, 1) = g(\zeta), \quad (57)$$

$$j = 0 \Rightarrow \theta(\zeta, 0) = \theta_0(\zeta) \quad \text{and} \quad j = 1 \Rightarrow \theta(\zeta, 1) = \theta(\zeta), \quad (58)$$

$$j = 0 \Rightarrow \varphi(\zeta, 0) = \varphi_0(\zeta) \quad \text{and} \quad j = 1 \Rightarrow \varphi(\zeta, 1) = \varphi(\zeta). \quad (59)$$

$f(\zeta, j)$ becomes $f_0(\zeta)$ and $f(\zeta)$ as j assumes the values zero and one. $g(\zeta, j)$ becomes $g_0(\zeta)$ and $g(\zeta)$ as j assumes the values zero and one. $\theta(\zeta, j)$ becomes $\theta_0(\zeta)$ and $\theta(\zeta)$ as j assumes the values zero and one. Finally, $\varphi(\zeta, j)$ becomes $\varphi_0(\zeta)$ and $\varphi(\zeta)$ as j assumes the values zero and one.

Applying Taylor series expansion on the Equations (56)–(59), the results are obtained as

$$f(\zeta, j) = f_0(\zeta) + \sum_{m=1}^{\infty} f_m(\zeta)j^m, \quad f_m(\zeta) = \frac{1}{m!} \frac{\partial^m f(\zeta, j)}{\partial j^m} \Big|_{j=0}, \tag{60}$$

$$g(\zeta, j) = g_0(\zeta) + \sum_{m=1}^{\infty} g_m(\zeta)j^m, \quad g_m(\zeta) = \frac{1}{m!} \frac{\partial^m g(\zeta, j)}{\partial j^m} \Big|_{j=0}, \tag{61}$$

$$\theta(\zeta, j) = \theta_0(\zeta) + \sum_{m=1}^{\infty} \theta_m(\zeta)j^m, \quad \theta_m(\zeta) = \frac{1}{m!} \frac{\partial^m \theta(\zeta, j)}{\partial j^m} \Big|_{j=0}, \tag{62}$$

$$\varphi(\zeta, j) = \varphi_0(\zeta) + \sum_{m=1}^{\infty} \varphi_m(\zeta)j^m, \quad \varphi_m(\zeta) = \frac{1}{m!} \frac{\partial^m \varphi(\zeta, j)}{\partial j^m} \Big|_{j=0}. \tag{63}$$

$\hbar_\varphi, \hbar_f, \hbar_\theta$ and \hbar_g are adjusted to obtain the convergence for the series in Equations (60)–(63) at $j = 1$, so Equations (60)–(63) transform to

$$f(\zeta) = f_0(\zeta) + \sum_{m=1}^{\infty} f_m(\zeta), \tag{64}$$

$$g(\zeta) = g_0(\zeta) + \sum_{m=1}^{\infty} g_m(\zeta), \tag{65}$$

$$\theta(\zeta) = \theta_0(\zeta) + \sum_{m=1}^{\infty} \theta_m(\zeta), \tag{66}$$

$$\varphi(\zeta) = \varphi_0(\zeta) + \sum_{m=1}^{\infty} \varphi_m(\zeta). \tag{67}$$

3.2. *m*th Order Deformation Problems

Considering Equations (48) and (52) for homotopy at *m*th order as

$$\mathbf{L}_f[f_m(\zeta) - \chi_m f_{m-1}(\zeta)] = \hbar_f R_m^f(\zeta), \tag{68}$$

$$f_m(0) = 0, \quad f_m(1) = 0, \quad f'_m(0) = 0, \quad f'_m(1) = 0, \tag{69}$$

$$R_m^f(\zeta) = B_1 f_{m-1}'''' + Re \left[\sum_{k=0}^{m-1} f_{m-1-k} f_k'''' + 2g_{m-1-k} g'_k - MB_2 f_{m-1}'' \right] - k_2 Re B_1 f_{m-1}' - 2k_3 Re \frac{1}{\rho_{hnf}} \sum_{k=0}^{m-1} f'_{m-1-k} f_k'''. \tag{70}$$

Considering Equations (49) and (53) for homotopy at *m*th order as

$$\mathbf{L}_g[g_m(\zeta) - \chi_m g_{m-1}(\zeta)] = \hbar_g R_m^g(\zeta), \tag{71}$$

$$g_m(0) = 0, \quad g_m(1) = 0, \tag{72}$$

$$R_m^g(\zeta) = B_1 g_{m-1}'' + Re \left[\sum_{k=0}^{m-1} 2f_{m-1-k} g'_k - MB_2 g'_{m-1} \right] - k_2 B_1 g_{m-1} - k_3 \frac{1}{\rho_{hnf}} \sum_{k=0}^{m-1} g_{m-1-k} g_k. \tag{73}$$

Considering Equations (50) and (54) for homotopy at *m*th order as

$$\mathbf{L}_\theta[\theta_m(\zeta) - \chi_m \theta_{m-1}(\zeta)] = \hbar_\theta R_m^\theta(\zeta), \tag{74}$$

$$\theta_m(0) = 0, \quad \theta_m(1) = 0, \tag{75}$$

$$R_m^\theta(\zeta) = B_3 \frac{k_{hmf}}{k_f} \theta''_{m-1} + \frac{1}{Rd} PrRe \left[2 \sum_{k=0}^{m-1} f_{m-1-k} \theta'_k + MB_4 Ec \left[\sum_{k=0}^{m-1} f'_{m-1-k} f'_k + \sum_{k=0}^{m-1} g_{m-1-k} g_k \right] \right]. \quad (76)$$

Considering Equations (51) and (55) for homotopy at m th order as

$$L_\varphi[\varphi_m(\zeta) - \chi_m \varphi_{m-1}(\zeta)] = \hbar_\varphi R_m^\varphi(\zeta), \quad (77)$$

$$\varphi'_m(0) = 0, \quad \varphi_m(1) = 0, \quad (78)$$

$$R_m^\varphi(\zeta) = \varphi''_{m-1} + ReSc \left[2 \sum_{k=0}^{m-1} f_{m-1-k} \varphi'_k + k_4 \left[\varphi_{m-1} + \varphi_{m-1-k} \sum_{l=0}^k \varphi_{k-l} \varphi_l - 2 \sum_{k=0}^{m-1} \varphi_{m-1-k} \varphi_k \right] \right], \quad (79)$$

$$\chi_m = \begin{cases} 0, & m \leq 1 \\ 1, & m > 1. \end{cases} \quad (80)$$

Adding the particular solutions $f_m^*(\zeta)$, $g_m^*(\zeta)$, $\theta_m^*(\zeta)$ and $\varphi_m^*(\zeta)$, Equations (68), (71), (74) and (77) yield the general solutions as

$$f_m(\zeta) = f_m^*(\zeta) + E_1 + E_2 \zeta + E_3 \zeta^2 + E_4 \zeta^3, \quad (81)$$

$$g_m(\zeta) = g_m^*(\zeta) + E_5 + E_6 \zeta, \quad (82)$$

$$\theta_m(\zeta) = \theta_m^*(\zeta) + E_7 + E_8 \zeta, \quad (83)$$

$$\varphi_m(\zeta) = \varphi_m^*(\zeta) + E_9 + E_{10} \zeta. \quad (84)$$

4. Results and Discussion

Results and discussion provide the analysis of the problem through the impacts of all the relevant parameters. The non-dimensional Equations (20), (22), (28) and (30) with boundary conditions in Equations (25), (26) and (29) are analytically computed. The performances of different parameters on the velocity profiles with heat and concentration of homogeneous-heterogeneous chemical reactions are shown in the relevant graphs. The streamlines show the internal behaviors of flow. The physical representation of the problem is shown in Figure 1. Liao [61] introduced \hbar -curves for the convergence of the series solution to get the precise and convergent solutions of the problems. \hbar -curves are also called the convergence controlling parameters for solution in the homotopy analysis method (used for solution in the present case). These \hbar -curves specify the range of numerical values. These numerical values (optimum values) are selected from the valid region in straight line. These optimum values of \hbar -curves are selected from the straight lines parallel to the horizontal axis (please see carefully Figures 2–5) to control the convergence of problem solution. In the present case, the valid region of each profile \hbar -curve is specified. Therefore, the admissible \hbar -curves for $f(\zeta)$, $g(\zeta)$, $\theta(\zeta)$ and $\varphi(\zeta)$ are drawn in the ranges $-10.00 \leq \hbar_f \leq -4.00$, $-10.00 \leq \hbar_g \leq -5.00$, $-3.5 \leq \hbar_\theta \leq -2.50$ and $-1.50 \leq \hbar_\varphi \leq -0.50$ in Figures 2–5, respectively.

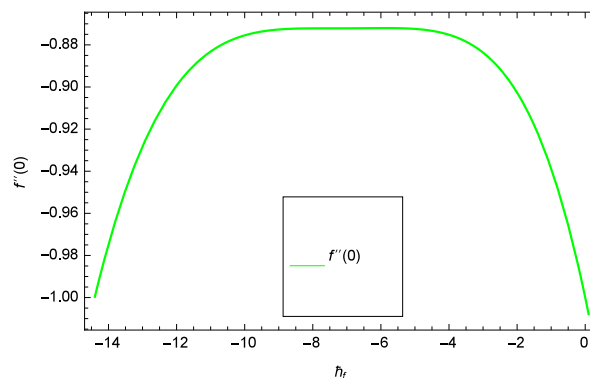


Figure 2. Illustration of the \hbar_f -curve of $f(\zeta)$.

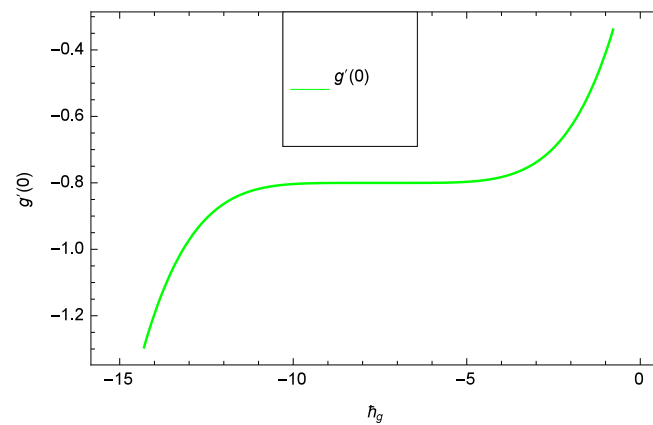


Figure 3. Illustration of the h_g -curve of $g(\zeta)$.

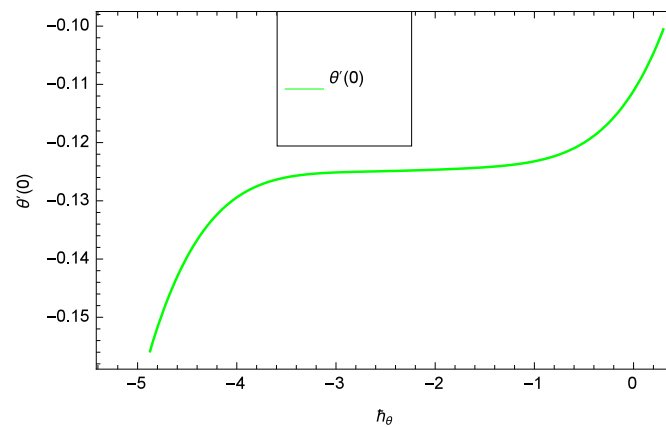


Figure 4. Illustration of the h_θ -curve of $\theta(\zeta)$.

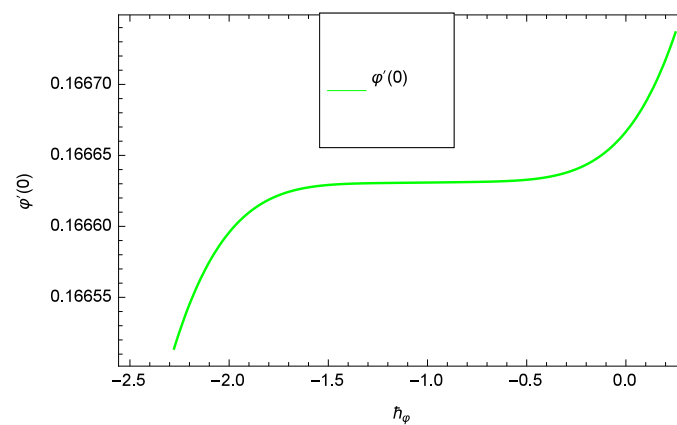


Figure 5. Illustration of the h_ϕ -curve of $\varphi(\zeta)$.

4.1. Axial Velocity Profile

In the present study, two nanofluids namely ZnO-C₂H₆O₂ and Au-ZnO/C₂H₆O₂ are investigated whose behaviors are shown through the graphs under the effects of different parameters. In Figures 6–25, the green and magenta colors are used for ZnO-C₂H₆O₂ and Au-ZnO/C₂H₆O₂ while in Figures 24 and 25, the additional colors are also used. There are solid and dashed curves in Figures 6–23. The mechanism is that three positive increasing numerical values are given to one parameter in the HAM solution while all the remaining parameters are fixed to show the effect of that

one parameter simultaneously on the two nanofluids namely ZnO-C₂H₆O₂ and Au-ZnO/C₂H₆O₂. When the solid lines locate below the dashed lines, then it shows the increasing effect and when the solid lines locate above the dashed lines, then it shows the decreasing effect. When the arrow head is from top to bottom, it shows the decreasing effect and when the arrow head is from bottom to top, it shows the increasing effect.

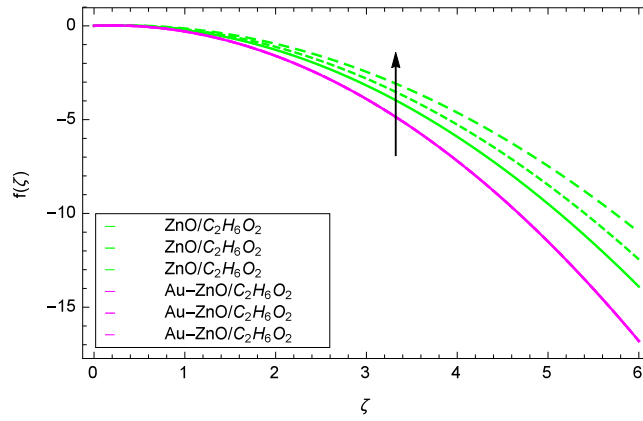


Figure 6. Illustration for the velocity $f(\zeta)$ and parameter $Re = 1.00, 1.50, 2.00$.

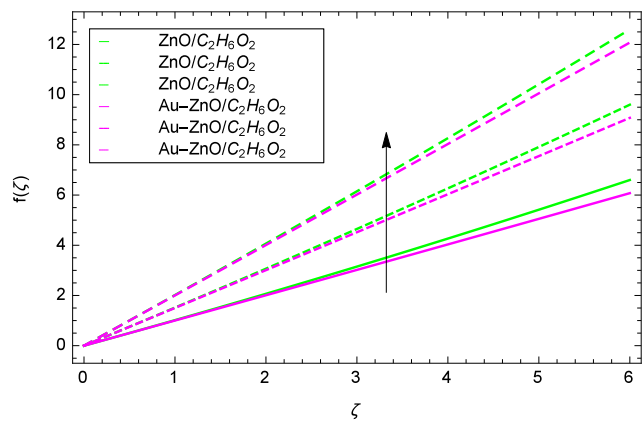


Figure 7. Illustration for the velocity $f(\zeta)$ and parameter $k_6 = 1.00, 1.50, 2.00$.

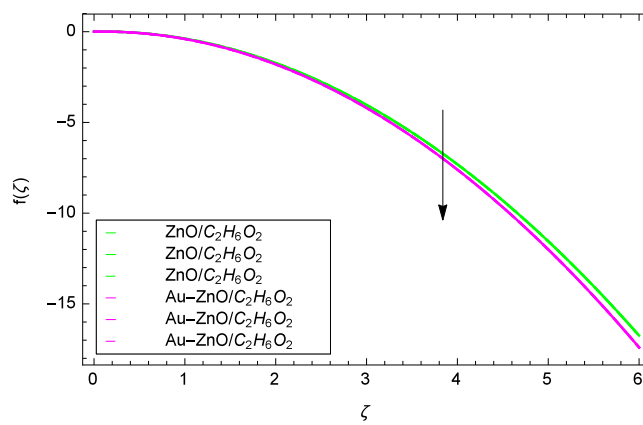


Figure 8. Illustration for the velocity $f(\zeta)$ and parameter $M = 1.00, 1.50, 2.00$.

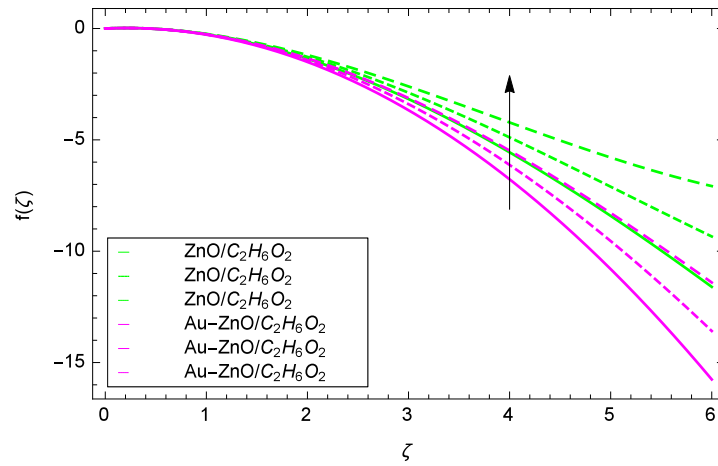


Figure 9. Illustration for the velocity $f(\zeta)$ and parameter $\Omega = 1.00, 1.50, 2.00$.

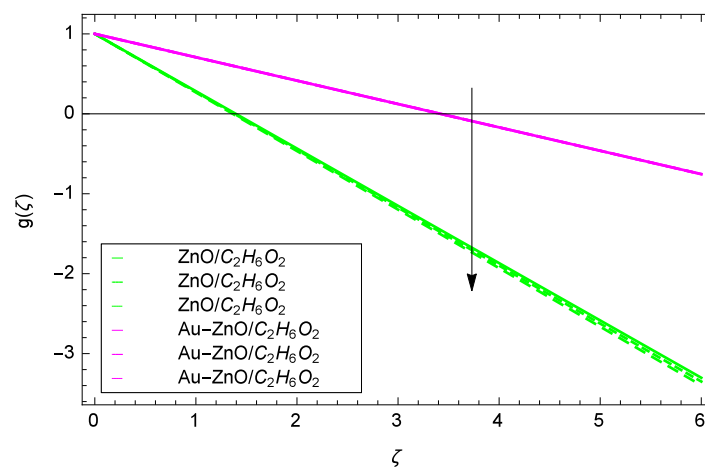


Figure 10. Illustration for the velocity $g(\zeta)$ and parameter $Re = 1.00, 10.50, 20.00$.

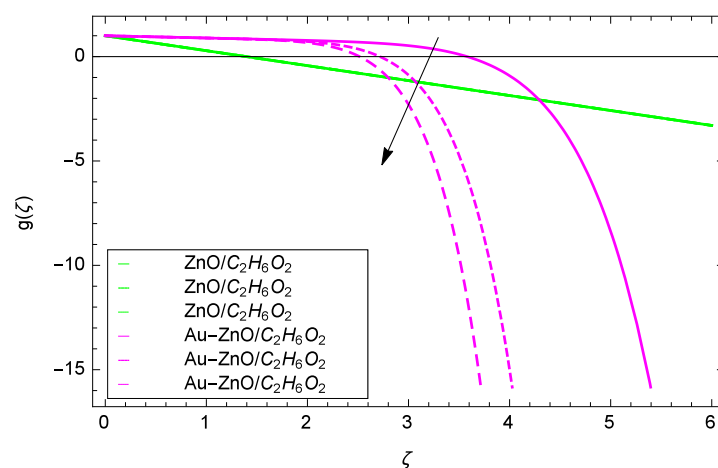


Figure 11. Illustration for the velocity $g(\zeta)$ and parameter $k_6 = 1.00, 10.50, 20.00$.

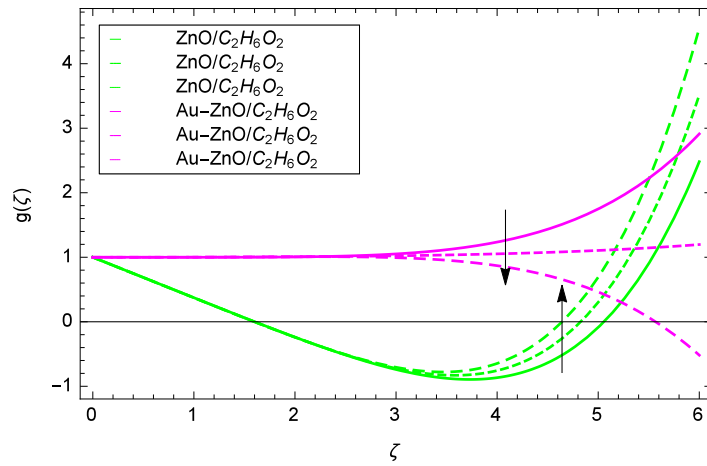


Figure 12. Illustration for the velocity $g(\zeta)$ and parameter $M = 1.00, 10.50, 20.00$.

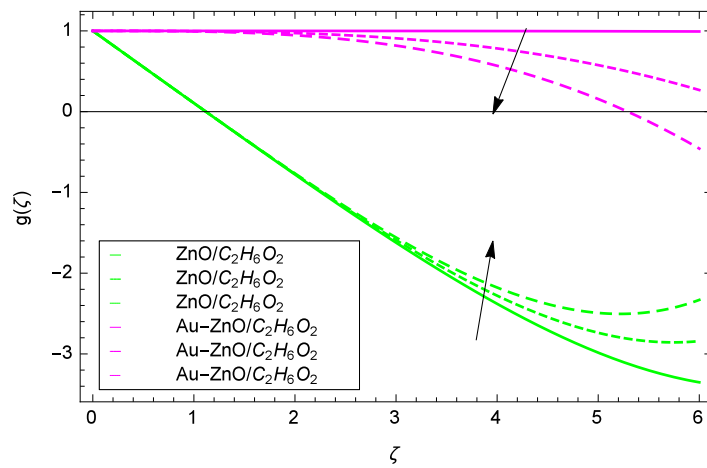


Figure 13. Illustration for the velocity $g(\zeta)$ and parameter $\Omega = 1.00, 1.50, 2.00$.

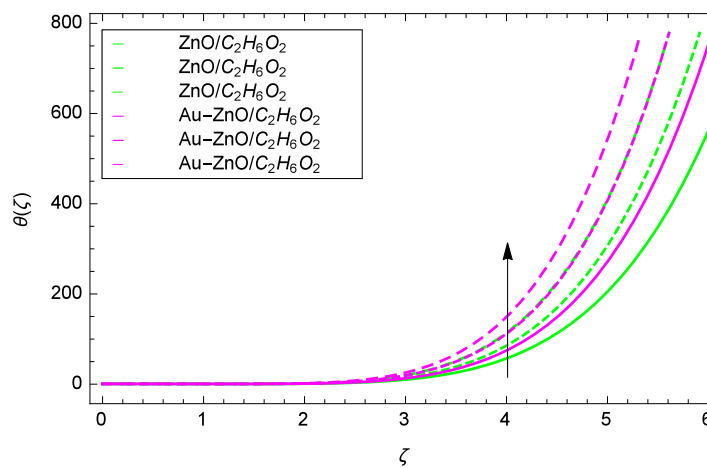


Figure 14. Illustration for the heat transfer $\theta(\zeta)$ and parameter $Re = 1.00, 1.50, 2.00$.

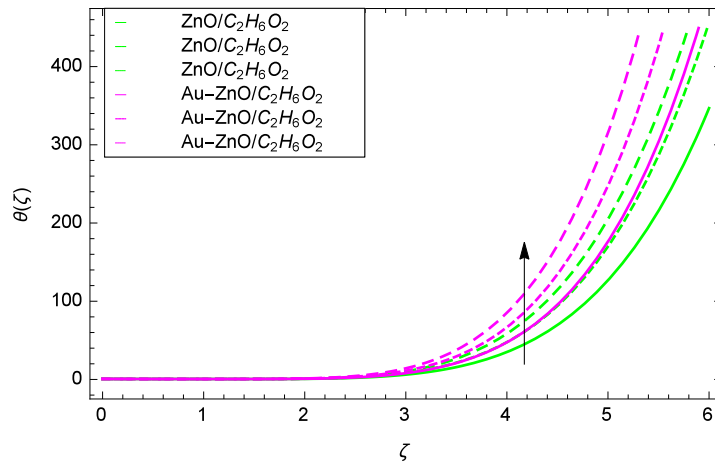


Figure 15. Illustration for the heat transfer $\theta(\zeta)$ and parameter $k_6 = 1.00, 1.50, 2.00$.

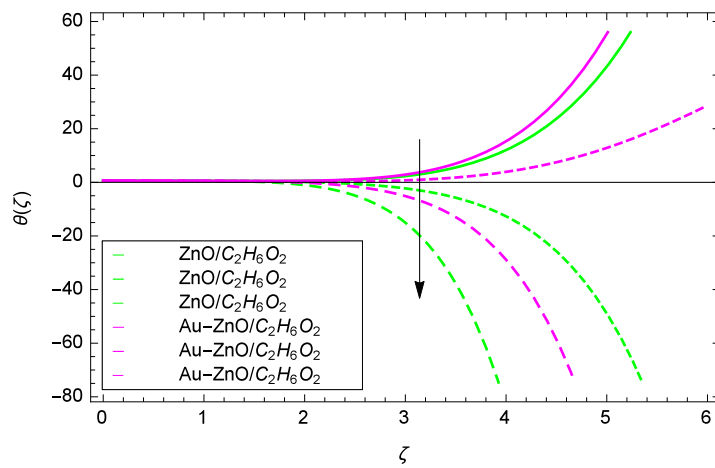


Figure 16. Illustration for the heat transfer $\theta(\zeta)$ and parameter $\Omega = 1.00, 5.50, 10.00$.

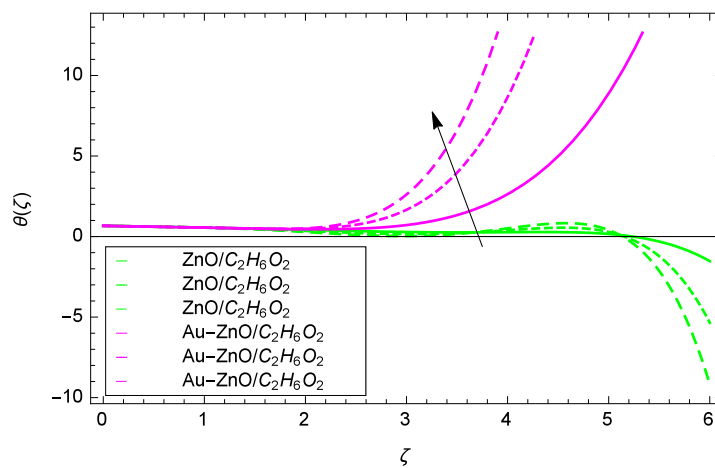


Figure 17. Illustration for the heat transfer $\theta(\zeta)$ and parameter $Pr = 1.00, 3.50, 6.00$.

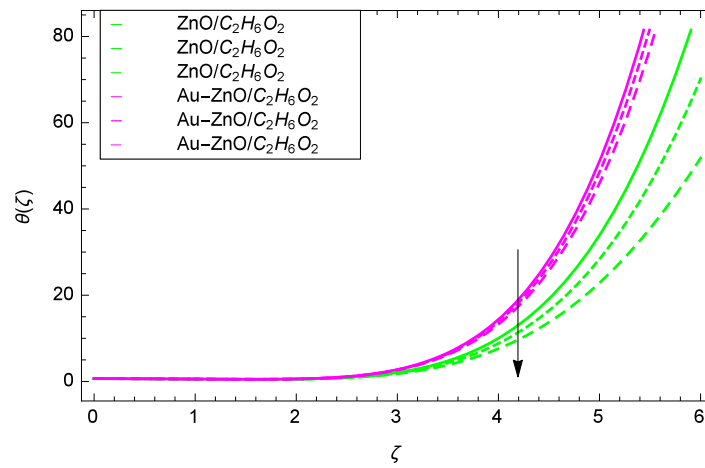


Figure 18. Illustration for the heat transfer $\theta(\zeta)$ and parameter $M = 1.00, 1.50, 2.00$.

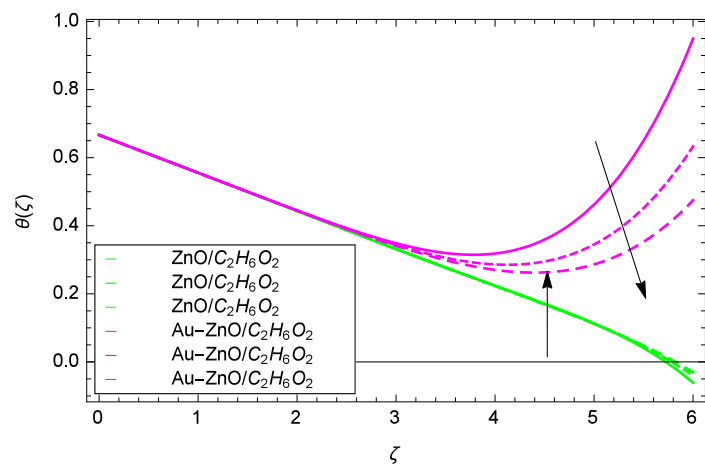


Figure 19. Illustration for the heat transfer $\theta(\zeta)$ and parameter $Rd = 1.00, 1.50, 2.00$.

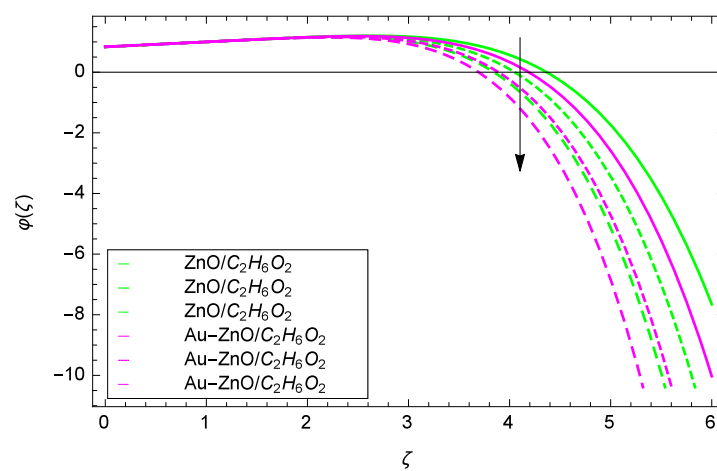


Figure 20. Illustration for the concentration $\varphi(\zeta)$ and parameter $Re = 1.00, 1.50, 2.00$.

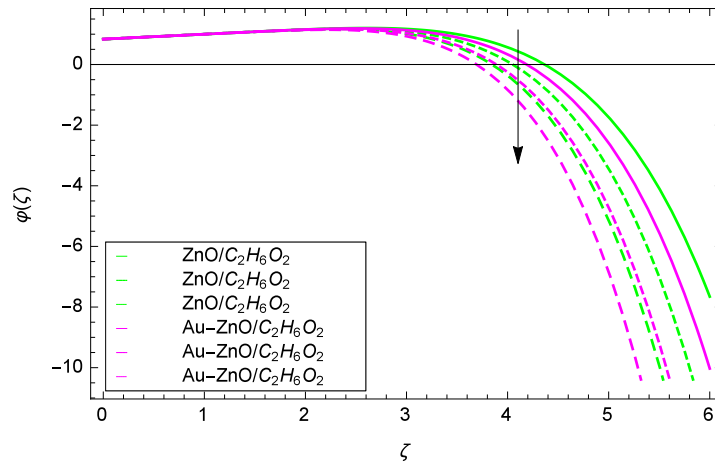


Figure 21. Illustration for the concentration $\varphi(\zeta)$ and parameter $k_4 = 1.00, 1.50, 2.00$.

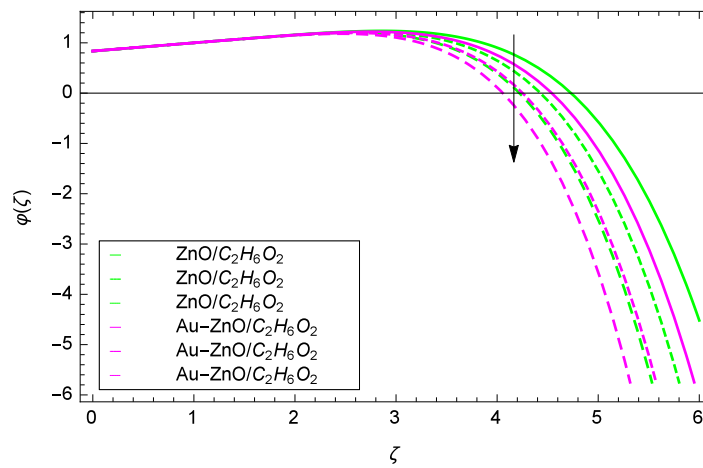


Figure 22. Illustration for the concentration $\varphi(\zeta)$ and parameter $k_6 = 1.00, 1.50, 2.00$.

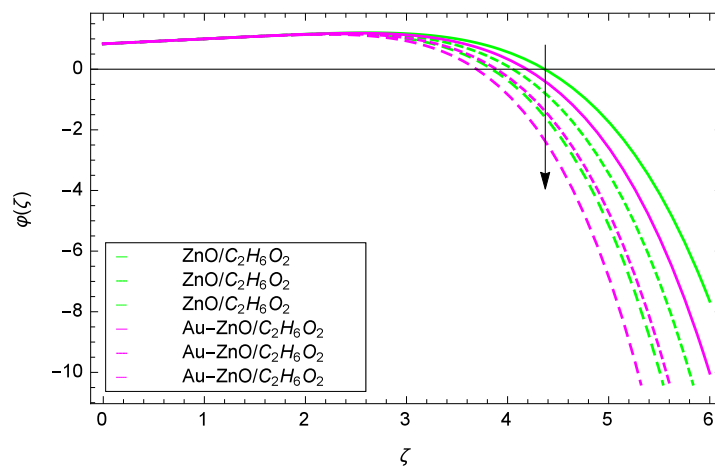


Figure 23. Illustration for the concentration $\varphi(\zeta)$ and parameter $Sc = 1.00, 1.50, 2.00$.

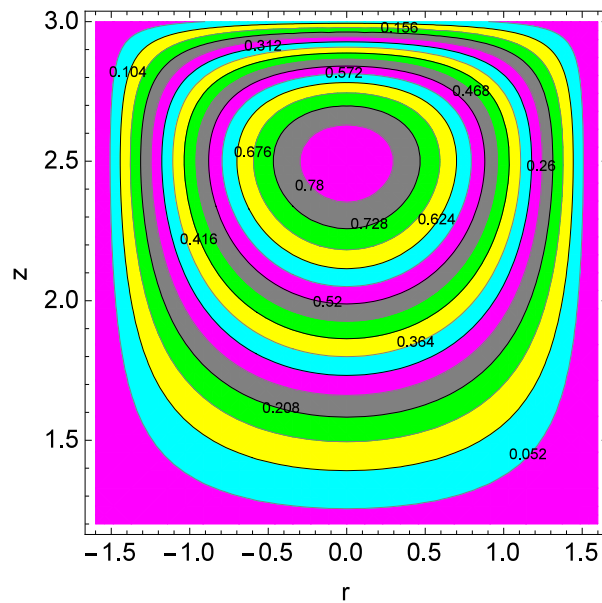


Figure 24. Illustration for the streamlines at upper disk and parameter $Re = 0.30$.

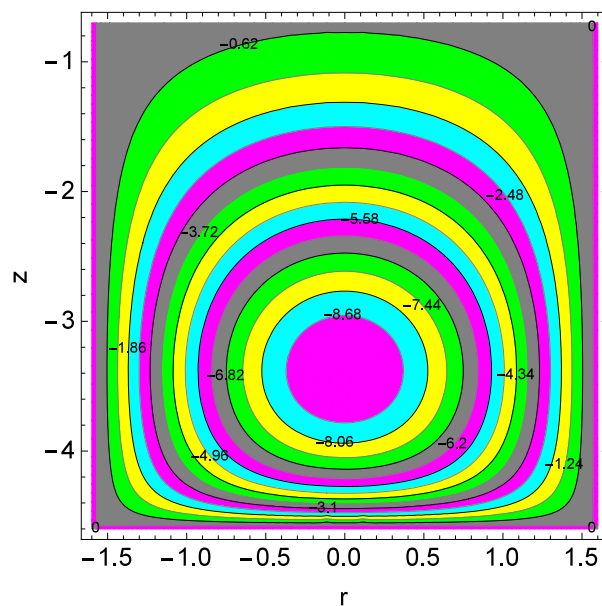


Figure 25. Illustration for the streamlines for lower disks and parameter $Re = 0.30$.

Figure 6 shows that for the different values of Reynolds number Re , the axial velocity $f(\zeta)$ is increased. In fact, the velocity of $ZnO-C_2H_6O_2$ and $Au-ZnO/C_2H_6O_2$ increase with increasing values of Reynolds number therefore overall motion is accelerated. Figure 7 shows the prominent role of stretching parameter k_6 due to lower disk in which the axial velocity $f(\zeta)$ increases. The present motion is due to stretching so if the stretching parameter is increased, the flow of fluids is also increased. In the mean time, porosity is responsible to decrease the axial flow. It shows that motion due to different nanofluids is reduced because the permeability at the edge of the accelerating surface increases. Surely, it is noted that excess of nanoparticles concentration is involved in decelerating the motion. It is worthy of notice that the axial velocity $f(\zeta)$ decreases against the inertia. Physically it means that the absorbency of the porous medium shows an increment in the thickness of the fluid. Figure 8 shows that magnetic field parameter resists the flow since due to magnetic field, the Lorentz forces are generated which resist the motion. The curves are shrink in response to the parameter effect. Figure 9 exhibits all

the assigned values of Ω and axial velocity $f(\zeta)$ which offers opportunities to know about the rotating systems and shows that the flow of ZnO-C₂H₆O₂ and Au-ZnO/C₂H₆O₂ increase.

Some interesting results have been found in case of tangential velocity $g(\zeta)$. Figure 10 shows that as the Reynolds number Re increases, the opposite tendency has been observed in the motion of ZnO-C₂H₆O₂ and Au-ZnO/C₂H₆O₂. The flow of mono nanofluid ZnO-C₂H₆O₂ decreases while the flow of hybrid nanofluid Au-ZnO/C₂H₆O₂ shows no prominent change for increasing the Reynolds number Re . In Figure 11, the tangential velocity $f(\zeta)$ tends to decreasing. Tangential velocity assumes a likely downfall so the flow is not supported by stretching due to k_6 . Figure 12 witnesses that the tangential velocity $g(\zeta)$ shifts to the effective decreasing for hybrid nanofluid Au-ZnO/C₂H₆O₂ and increases for ZnO-C₂H₆O₂ on behalf of the magnetic field parameter M . Figure 13 exhibits that rotation parameter Ω parameter resists the tangential flow of Au-ZnO/C₂H₆O₂ and enhances the tangential flow of ZnO-C₂H₆O₂.

4.2. Temperature Profile

Figure 14 shows the effect of Reynolds number Re on heat transfer. The larger values of Re increase the temperature of ZnO-C₂H₆O₂ and Au-ZnO/C₂H₆O₂. It has been observed in Figure 15 that as the stretching parameter k_6 increases, the temperature of ZnO-C₂H₆O₂ and Au-ZnO/C₂H₆O₂ increase. These observations indicate that the fluid temperature and its related layer are incremented for higher estimations of k_6 . The rotation parameter Ω cannot generate an extra heating to the system as shown in Figure 16. Temperature $\theta(\zeta)$ is decreased on increasing the parameter Ω . The physical reason is that enhancement in Ω causes to improve the internal source of energy, that is why the fluid temperature is reduced. The system gets the parameter Pr for the designated values 1.00, 3.50, and 6.00 during the process and increases the temperature shown through Figure 17. The direct relation of Pr and thermal conductivity increases the thickness of thermal boundary layer. Larger values of Pr generate the high diffusion of heat transfer. The temperature $\theta(\zeta)$ is changed to lowest level after the exchange of high values of magnetic field parameter M as shown in Figure 18. The reason is that strong Lorentz forces resist the flow of nanoparticles, so causing no high collision among the nanoparticles, consequently, the temperature is decreased. Figure 19 depicts that with the increasing values of thermal radiation parameter Rd , the temperature $\theta(\zeta)$ of ZnO-C₂H₆O₂ increases while the temperature of hybrid nanofluid Au-ZnO-C₂H₆O₂ decreases. The reason is that radiation enhances more heat in the working fluids.

4.3. Concentration of Homogeneous-Heterogeneous Chemical Reactions

Looking at the non-dimensional Equation (28), the suitable values of Re , Sc and k_4 are the basic quantities for generating a cubic autocatalysis chemical reaction. The concentration of chemical reaction $\varphi(\zeta)$ is low with the Reynolds number Re as shown in Figure 20. Figure 21 shows that for the homogeneous chemical reaction parameter k_4 , the concentration of chemical reaction is decreased. From Equation (28), it is witnessed that the homogeneous chemical reaction parameter k_4 is a part of performance with the multiple solutions. Enhancement in k_4 makes dominant the concentration. In Figure 22, the stretching parameter k_6 upgrades concentration of chemical reaction with low level by performing active role in the rotating motion. The stretching parameter k_6 makes compact the homogeneous reaction and hence the concentration profile $\varphi(\zeta)$. Figure 23 stands for the outcomes of Schmidt number Sc and concentration $\varphi(\zeta)$. Momentum diffusivity to mass diffusivity is known as Schmidt number. The parameter Sc causes to make low the homogeneous chemical reaction.

4.4. Streamlines

Figure 24 shows the streamlines at upper disks. The size of the streamlines increases at upper disk compared to that of lower disk. Both mono nanofluid and hybrid nanofluid proceed towards the edges of disks. Figure 25 shows the streamlines for the Reynolds number Re at lower disks. The compression of streamlines are clear from Figure 25. The plumes power is strong for lower disks.

4.5. Authentication of the Present Work

The important physical quantities introduced in Section 2 are evaluated to compare the validity of the solution with the published work [8]. Table 4 shows the tabulations to the several values for the parameter Re . There exists a nice agreement with the published work [8]. Similarly in Table 5, the values of heat transfer rate are computed for the volume fraction $\phi = 0.10, 0.20, 0.30,$ and 0.40 . These values also have the close agreement with the published work [8].

Table 4. Comparison of the present and published work.

Reynolds Number (Re)	$f''(1)$ [8]	$f''(1)$ (Present)	$g'(1)$ [8]	$g'(1)$ (Present)
0.10	0.292991	0.292993	0.284684	0.284683
0.20	0.237792	0.237791	0.224995	0.224994
0.30	0.208284	0.208283	0.197046	0.197044
0.40	0.206995	0.206994	0.203117	0.203115

Table 5. Comparison of the present and published work.

Volume Fraction (ϕ)	$-\theta'(0)$ [8]	$-\theta'(0)$ (Present)	$-\theta'(1)$ [8]	$-\theta'(1)$ (Present)
0.10	3.677172	3.677170	2.26814	2.26813
0.20	4.53192	4.53190	3.128083	3.128081
0.30	2.983936	2.983935	1.648859	1.648857
0.40	3.00208	3.00207	1.624995	1.624993

5. Conclusions

A significant modification in the mathematical model for hybrid nanofluid has been made for the analysis of flow, heat and mass transfer. Chemical species reactions are shown in hybrid nanofluid. The problem is modeled in rotating systems for the nanoparticles ZnO and Au with base fluid ethylene glycol and solved through HAM. In ethylene glycol-based fluid ($C_2H_6O_2$), two types of nanoparticles, namely ZnO (zinc oxide) and Au (gold), with volume fractions $\phi_1 = 0.03$ and $\phi_2 = 0.04$ are investigated, respectively. It is noted that for $\phi_1 = 0.00$ and $\phi_2 = 0.00$, the problem becomes about viscous fluid with the absence of nanoparticles volume fractions. If $\phi_1 = 0.00$, $Ag/C_2H_6O_2$ is obtained and if $\phi_2 = 0.00$, $ZnO_2/C_2H_6O_2$ is constructed. Achieving better comprehension, the competencies of active parameters on flow, heat transfer and concentration of heterogeneous-homogeneous chemical reactions are noted. There exists a nice agreement between the present and published work in Tables 4 and 5. The problem has potential for renewable energy system and researchers to investigate the thermal conductivity of nanoparticles like silver, aluminum, copper etc. with different base fluids like water, benzene, engine oil etc. The results for flow, heat transfer and concentration of homogeneous-heterogeneous chemical reactions are summarized as following.

- (1) Axial velocity $f(\zeta)$ increases for ZnO- $C_2H_6O_2$ and Au-ZnO/ $C_2H_6O_2$ with the increasing values of Reynolds number Re , stretching parameter k_6 and rotation parameter Ω while axial velocity $f(\zeta)$ decreases for ZnO- $C_2H_6O_2$ and Au-ZnO/ $C_2H_6O_2$ with the increasing values of magnetic field parameter M .
- (2) Tangential velocity $g(\zeta)$ increases for ZnO- $C_2H_6O_2$ with the increasing values of magnetic field parameter M and rotation parameter Ω while the same velocity decreases for Au-ZnO/ $C_2H_6O_2$ with the increasing values of magnetic field parameter M and rotation parameter Ω . Moreover, tangential velocity $g(\zeta)$ decreases for ZnO- $C_2H_6O_2$ and Au-ZnO/ $C_2H_6O_2$ with the increasing values of Reynolds number Re and stretching parameter k_6 .
- (3) Heat transfer $\theta(\zeta)$ increases for ZnO- $C_2H_6O_2$ and Au-ZnO/ $C_2H_6O_2$ with the increasing values of Reynolds number Re , stretching parameter k_6 . Similarly, heat transfer $\theta(\zeta)$ increases for ZnO- $C_2H_6O_2$ with increasing values of thermal radiation parameter Rd while it is decreased for ZnO- $C_2H_6O_2$ and Au-ZnO/ $C_2H_6O_2$ with the increasing values of rotation parameter Ω , magnetic

- field parameter M . In case of Au-ZnO/C₂H₆O₂, heat transfer $\theta(\zeta)$ also decreases with increasing values of thermal radiation parameter Rd .
- (4) The concentration of homogeneous-heterogeneous chemical reactions $\varphi(\zeta)$ decreases for ZnO-C₂H₆O₂ and Au-ZnO/C₂H₆O₂ with the increasing values of Reynolds number Re , stretching parameter k_6 and Schmidt number Sc .
 - (5) Streamlines are compressed at the upper portion of upper disk while these are compressed at the lower portion of lower disk when the Reynolds number Re assumes the value 0.30.
 - (6) Tables 4 and 5 show an excellent agreement of the present work with published work.

Author Contributions: Conceptualization, N.S.K.; methodology, N.S.K.; software, N.S.K.; validation, N.S.K.; formal analysis, P.K.; investigation, N.S.K.; resources, P.T.; data curation, P.T.; writing—original draft preparation, N.S.K.; writing—review and editing, N.S.K.; visualization, P.K.; supervision, N.S.K.; project administration, P.K.; funding acquisition, P.K. All authors have read and agreed to the revised version of the manuscript.

Funding: This research is funded by the Center of Excellence in Theoretical and Computational Science (TaCS-CoE), KMUTT.

Acknowledgments: This work was partially supported by the International Research Partnerships: Electrical Engineering Thai-French Research Center (EE-TFRC) between King Mongkut's University of Technology North Bangkok and Universite' de Lorraine under Grant KMUTNB-BasicR-64-17. The authors are cordially thankful to the honorable reviewers for their constructive comments to improve the quality of the paper. This research is supported by the Postdoctoral Fellowship from King Mongkut's University of Technology Thonburi (KMUTT), Thailand. This project is supported by the Theoretical and Computational Science (TaCS) Center under Computational and Applied Science for Smart Innovation Research Cluster (CLASSIC), Faculty of Science, KMUTT.

Conflicts of Interest: The authors declare no conflict of interest.

References

1. Kasaeian, A.; Eshghi, A.T.; Sameti, M. A review on the applications of nanofluids in solar energy systems. *Renew. Sustain. Energy Rev.* **2015**, *43*, 584–598. [[CrossRef](#)]
2. Etefagh, E.; Ghobadian, B.; Rashidi, S.; Najafi, G.; Khoshtaghaza, M.H.; Rashtchi, M.; Sadeghian, S. A novel bio-nano emulsion fuel based on biodegradable nanoparticles to improve diesel engines performance and reduce exhaust emissions. *Renew. Energy* **2018**, *125*, 64–72. [[CrossRef](#)]
3. Gunjo, D.G.; Jena, S.R.; Mahanta, P.; Robi, P.S. Melting enhancement of a latent heat storage with dispersed Cu, CuO and Al₂O₃ nanoparticles for solar thermal application. *Renew. Energy* **2018**, *121*, 652–665. [[CrossRef](#)]
4. Khanafer, K.; Vafi, K. A review on the applications of nanofluids in solar energy field. *Renew. Energy* **2018**, *123*, 398–406. [[CrossRef](#)]
5. Caglar, M.; Ilican, S.; Caglar, Y.; Yakuphanoglu, F. Electrical conductivity and optical properties of ZnO nanostructured thin film. *Appl. Surf. Sci.* **2009**, *225*, 4491–4496. [[CrossRef](#)]
6. Islam, R.I.; Shabani, B.; Rosengarten, G. Electrical and thermal conductivities of water-ethylene glycol based TiO₂ nanofluids to be used as coolants in PEM fuel cells. *Energy Procedia* **2017**, *110*, 101–108. [[CrossRef](#)]
7. Fal, J.; Sidorowicz, A.; Zyla, G. Electrical conductivity of ethylene glycol based nanofluids with different types of thulium oxide nanoparticles. *Acta Phys. Pol. A* **2017**, *132*, 146–148. [[CrossRef](#)]
8. Rout, B.C.; Mishra, S.R.; Nayak, B. Semi analytical solution of axisymmetric flows of Cu- and Ag-water nanofluids between two rotating disks. *Heat Transf. Asian Res.* **2019**, *132*, 1–25. [[CrossRef](#)]
9. Hamilton, R.L.; Crosser, O.K. Thermal conductivity of heterogeneous two component systems. *Ind. Eng. Chem. Fundam.* **1962**, *1*, 187–191. [[CrossRef](#)]
10. Choi, S.U.S.; Eastman, J.A. Enhancing thermal conductivity of fluids with nanoparticles. In Proceedings of the 1995 International Mechanical Engineering Congress and Exhibition, San Francisco, CA, USA, 12–17 November 1995; Volume 231, pp. 99–106.
11. Vallejo, J.P.; Zyla, G.; Fernandez-Seara, J.; Lugo, L. Influence of six carbon-based nanomaterials on the rheological properties of nanofluids. *Nanomaterials* **2019**, *9*, 146. [[CrossRef](#)]
12. Alihosseini, S.; Jafari, A. The effect of porous medium configuration on nanofluid heat transfer. *Appl. Nanosci.* **2020**, *10*, 895–906. [[CrossRef](#)]

13. Sheikholeslami, M.; Shah, Z.; Tassaddiq, A.; Shafee, A.; Khan, I. Application of electric field for augmentation of Ferrofluid heat transfer in an enclosure including double moving walls. *IEEE Access* **2019**, *7*, 21048–21056. [[CrossRef](#)]
14. Al-Kouz, W.; Al-Muhtady, A.; Owhaib, W.; Al-Dahidi, S.; Hadar, M.; Abu-Alghanam, R. Entropy generation optimization for rarified nanofluid flows in a square cavity with two fins at the hot wall. *Entropy* **2019**, *21*, 103. [[CrossRef](#)]
15. Atta, A.M.; Abdullah, M.M.S.; Al-Lohedan, H.A.; Mohamed, N.H. Novel superhydrophobic sand and polyurethane sponge coated with silica/modified asphaltene nanoparticles for rapid oil spill cleanup. *Nanomaterials* **2019**, *9*, 187. [[CrossRef](#)]
16. Rout, A.; Boltaev, G.S.; Ganeev, R.A.; Fu, Y.; Maurya, S.K.; Kim, V.V.; Rao, K.S.; Guo, C. Nonlinear optical studies of gold nanoparticles films. *Nanomaterials* **2019**, *9*, 291. [[CrossRef](#)] [[PubMed](#)]
17. Alvarez-Regueiro, E.; Vallejo, J.P.; Fernandez-Seara, J.; Fernandez, J.; Lugo, L. Experimental convection heat transfer analysis of a nano-enhanced industrial coolant. *Nanomaterials* **2019**, *9*, 267. [[CrossRef](#)]
18. Alsagri, A.S.; Nasir, S.; Gul, T.; Islam, S.; Nisar, K.S.; Shah, Z.; Khan, I. MHD thin film flow and thermal analysis of blood with CNTs nanofluid. *Coatings* **2019**, *9*, 175. [[CrossRef](#)]
19. Mishra, S.K.; Chandra, H.; Arora, A. Effect of velocity and rheology of nanofluid on heat transfer of laminar vibrational flow through a pipe under constant heat flux. *Int. Nano Lett.* **2019**, *9*, 245–256. [[CrossRef](#)]
20. Abbas, S.Z.; Khan, W.A.; Sun, H.; Ali, M.; Irfan, M.; Shahzed, M.; Sultan, F. Mathematical modeling and analysis of cross nanofluid flow subjected to entropy generation. *Appl. Nanosci.* **2019**, *10*, 3149–3160. [[CrossRef](#)]
21. Ali, M.; Khan, W.A.; Irfan, M.; Sultan, F.; Shahzed, M.; Khan, M. Computational analysis of entropy generation for cross nanofluid flow. *Appl. Nanosci.* **2019**, *10*, 3045–3055. [[CrossRef](#)]
22. Sharma, R.P.; Seshadri, R.; Mishra, S.R.; Munjam, S.R. Effect of thermal radiation on magnetohydrodynamic three-dimensional motion of a nanofluid past a shrinking surface under the influence of a heat source. *Heat Transf. Asian Res.* **2019**, *48*, 2105–2121. [[CrossRef](#)]
23. Jahan, S.; Sakidin, H.; Nazar, R.; Pop, I. Analysis of heat transfer in nanofluid past a convectively heated permeable stretching/shrinking sheet with regression and stability analyses. *Results Phys.* **2018**, *10*, 395–405. [[CrossRef](#)]
24. Hossinzadeh, K.; Asadi, A.; Mogharrebi, A.R.; Khalesi, J.; Mousavisani, S.; Ganji, D.D. Entropy generation analysis of $(\text{CH}_2\text{OH})_2$ containing CNTs nanofluid flow under effect of MHD and thermal radiation. *Case Stud. Therm. Eng.* **2019**, *14*, 100482. [[CrossRef](#)]
25. Khan, N.S. Bioconvection in second grade nanofluid flow containing nanoparticles and gyrotactic microorganisms. *Braz. J. Phys.* **2018**, *43*, 227–241. [[CrossRef](#)]
26. Khan, N.S.; Gul, T.; Khan, M.A.; Bonyah, E.; Islam, S. Mixed convection in gravity-driven thin film non-Newtonian nanofluids flow with gyrotactic microorganisms. *Results Phys.* **2017**, *7*, 4033–4049. [[CrossRef](#)]
27. Khan, N.S.; Gul, T.; Islam, S.; Khan, I.; Alqahtani, A.M.; Alshomrani, A.S. Magnetohydrodynamic nanoliquid thin film sprayed on a stretching cylinder with heat transfer. *J. Appl. Sci.* **2017**, *7*, 271. [[CrossRef](#)]
28. Zuhra, S.; Khan, N.S.; Khan, M.A.; Islam, S.; Khan, W.; Bonyah, E. Flow and heat transfer in water based liquid film fluids dispensed with graphene nanoparticles. *Results Phys.* **2018**, *8*, 1143–1157. [[CrossRef](#)]
29. Khan, N.S.; Gul, T.; Islam, S.; Khan, W. Thermophoresis and thermal radiation with heat and mass transfer in a magnetohydrodynamic thin film second-grade fluid of variable properties past a stretching sheet. *Eur. Phys. J. Plus* **2017**, *132*, 11. [[CrossRef](#)]
30. Palwasha, Z.; Khan, N.S.; Shah, Z.; Islam, S.; Bonyah, E. Study of two dimensional boundary layer thin film fluid flow with variable thermo-physical properties in three dimensions space. *AIP Adv.* **2018**, *8*, 105318. [[CrossRef](#)]
31. Khan, N.S.; Gul, T.; Islam, S.; Khan, A.; Shah, Z. Brownian motion and thermophoresis effects on MHD mixed convective thin film second-grade nanofluid flow with Hall effect and heat transfer past a stretching sheet. *J. Nanofluids* **2017**, *6*, 812–829. [[CrossRef](#)]
32. Khan, N.S.; Zuhra, S.; Shah, Z.; Bonyah, E.; Khan, W.; Islam, S. Slip flow of Eyring-Powell nanoliquid film containing graphene nanoparticles. *AIP Adv.* **2019**, *8*, 115302. [[CrossRef](#)]
33. Khan, N.S.; Gul, T.; Kumam, P.; Shah, Z.; Islam, S.; Khan, W.; Zuhra, S.; Sohail, A. Influence of inclined magnetic field on Carreau nanoliquid thin film flow and heat transfer with graphene nanoparticles. *Energies* **2019**, *12*, 1459. [[CrossRef](#)]

34. Khan, N.S. Study of two dimensional boundary layer flow of a thin film second grade fluid with variable thermo-physical properties in three dimensions space. *Filomat* **2019**, *33*, 5387–5405. [[CrossRef](#)]
35. Khan, N.S.; Zuhra, S. Boundary layer unsteady flow and heat transfer in a second grade thin film nanoliquid embedded with graphene nanoparticles past a stretching sheet. *Adv. Mech. Eng.* **2019**, *11*, 1–11. [[CrossRef](#)]
36. Khan, N.S.; Gul, T.; Islam, S.; Khan, W.; Khan, I.; Ali, L. Thin film flow of a second-grade fluid in a porous medium past a stretching sheet with heat transfer. *Alex. Eng. J.* **2017**, *57*, 1019–1031. [[CrossRef](#)]
37. Zuhra, S.; Khan, N.S.; Alam, A.; Islam, S.; Khan, A. Buoyancy effects on nanoliquids film flow through a porous medium with gyrotactic microorganisms and cubic autocatalysis chemical reaction. *Adv. Mech. Eng.* **2020**, *12*, 1–17. [[CrossRef](#)]
38. Palwasha, Z.; Islam, S.; Khan, N.S.; Ayaz, H. Non-Newtonian nanoliquids thin film flow through a porous medium with magnetotactic microorganisms. *Appl. Nanosci.* **2018**, *8*, 1523–1544. [[CrossRef](#)]
39. Khan, N.S. Mixed convection in MHD second grade nanofluid flow through a porous medium containing nanoparticles and gyrotactic microorganisms with chemical reaction. *Filomat* **2019**, *33*, 4627–4653. [[CrossRef](#)]
40. Zuhra, S.; Khan, N.S.; Shah, Z.; Islam, Z.; Bonyah, E. Simulation of bioconvection in the suspension of second grade nanofluid containing nanoparticles and gyrotactic microorganisms. *AIP Adv.* **2018**, *8*, 105210. [[CrossRef](#)]
41. Khan, N.S.; Shah, Z.; Shutaywi, M.; Kumam, P.; Thounthong, P. A comprehensive study to the assessment of Arrhenius activation energy and binary chemical reaction in swirling flow. *Sci. Rep.* **2020**, *10*, 7868. [[CrossRef](#)]
42. Zuhra, S.; Khan, N.S.; Islam, S. Magnetohydrodynamic second grade nanofluid flow containing nanoparticles and gyrotactic microorganisms. *Comput. Appl. Math.* **2018**, *37*, 6332–6358. [[CrossRef](#)]
43. Zuhra, S.; Khan, N.S.; Islam, S.; Nawaz, R. Complexiton solutions for complex KdV equation by optimal homotopy asymptotic method. *Filomat* **2020**, *33*, 6195–6211. [[CrossRef](#)]
44. Zahra, A.; Mahanthesh, B.; Basir, M.F.M.; Imtiaz, M.; Mackolil, J.; Khan, N.S.; Nabwey, H.A.; Tlili, I. Mixed radiated magneto Casson fluid flow with Arrhenius activation energy and Newtonian heating effects: Flow and sensitivity analysis. *Alex. Eng. J.* **2020**, *57*, 1019–1031.
45. Liaqat, A.; Asifa, T.; Ali, R.; Islam, S.; Gul, T.; Kumam, P.; Mukhtar, S.; Khan, N.S.; Thounthong, P. A new analytical approach for the research of thin-film flow of magneto hydrodynamic fluid in the presence of thermal conductivity and variable viscosity. *ZAMM J. Appl. Math. Mech. Z. Angewandte Math. Mech.* **2020**, 1–13. [[CrossRef](#)]
46. Khan, N.S.; Zuhra, S.; Shah, Q. Entropy generation in two phase model for simulating flow and heat transfer of carbon nanotubes between rotating stretchable disks with cubic autocatalysis chemical reaction. *Appl. Nanosci.* **2019**, *9*, 1797–1822. [[CrossRef](#)]
47. Khan, N.S.; Shah, Z.; Islam, S.; Khan, I.; Alkanhal, T.A.; Tlili, I. Entropy generation in MHD mixed convection non-Newtonian second-grade nanoliquid thin film flow through a porous medium with chemical reaction and stratification. *Entropy* **2019**, *21*, 139. [[CrossRef](#)]
48. Khan, N.S.; Zuhra, S.; Shah, Z.; Bonyah, E.; Khan, W.; Islam, S.; Khan, A. Hall current and thermophoresis effects on magnetohydrodynamic mixed convective heat and mass transfer thin film flow. *J. Phys. Commun.* **2019**, *3*, 035009. [[CrossRef](#)]
49. Khan, N.S.; Kumam, P.; Thounthong, P. Renewable energy technology for the sustainable development of thermal system with entropy measures. *Int. J. Heat Mass Transf.* **2019**, *145*, 118713. [[CrossRef](#)]
50. Khan, N.S.; Kumam, P.; Thounthong, P. Second law analysis with effects of Arrhenius activation energy and binary chemical reaction on nanofluid flow. *Sci. Rep.* **2020**, *10*, 1226. [[CrossRef](#)]
51. Khan, N.S.; Shah, Q.; Bhaumik, A.; Kumam, P.; Thounthong, P.; Amiri, I. Entropy generation in bioconvection nanofluid flow between two stretchable rotating disks. *Sci. Rep.* **2020**, *10*, 4448. [[CrossRef](#)]
52. Khan, N.S.; Shah, Q.; Sohail, A. Dynamics with Cattaneo-Christov heat and mass flux theory of bioconvection Oldroyd-B nanofluid. *Adv. Mech. Eng.* **2020**. [[CrossRef](#)]
53. Khan, N.S.; Shah, Q.; Sohail, A.; Kumam, P.; Thounthong, P.; Bhaumik, A.; Ullah, Z. Lorentz forces effects on the interactions of nanoparticles in emerging mechanisms with innovative approach. *Symmetry* **2020**, *5*, 1700. [[CrossRef](#)]
54. Liaqat, A.; Khan, N.S.; Ali, R.; Islam, S.; Kumam, P.; Thounthong, P. Novel insights through the computational techniques in unsteady MHD second grade fluid dynamics with oscillatory boundary conditions. *Heat Transf.* **2020**. [[CrossRef](#)]

55. Khan, N.S.; Ali, L.; Ali, R.; Kumam, P.; Thounthong, P. A novel algorithm for the computation of systems containing different types of integral and integro-differential equations. *Heat Transf.* **2020**. [[CrossRef](#)]
56. Ahmad, S.; Nadeem, S.; Ullah, N. Entropy generation and temperature-dependent viscosity in the study of SWCNT-MWCNT hybrid nanofluid. *Appl. Nanosci.* **2020**. [[CrossRef](#)]
57. Dinarvand, S.; Rostami, M.N. An innovative mass-based model of aqueous zinc oxide-gold hybrid nanofluid for von Karman's swirling flow. *J. Therm. Anal. Calorim.* **2019**. [[CrossRef](#)]
58. Ahmed, S.; Xu, H. Mixed convection in gravity driven thin nano-liquid film flow with homogeneous-heterogeneous reactions. *Phys. Fluids* **2020**, *32*, 023604. [[CrossRef](#)]
59. Hayat, T.; Haider, F.; Muhammad, T.; Ahmad, B. Darcy-Forchheimer flow of carbon nanotubes due to a convectively heated rotating disk with homogeneous-heterogeneous chemical reactions. *J. Therm. Anal. Calorim.* **2019**, *137*, 1939–1949. [[CrossRef](#)]
60. Suleman, M.; Ramzan, M.; Ahmad, S.; Lu, D.; Muhammad, T.; Chung, J.D. A numerical simulation of silver-water nanofluid flow with impacts of Newtonian heating and homogeneous-heterogeneous reactions past a nonlinear stretched cylinder. *Symmetry* **2019**, *11*, 295. [[CrossRef](#)]
61. Liao, S.J. *Homotopy Analysis Method in Non-Linear Differential Equations*; Higher Education Press: Beijing, China; Springer: Berlin/Heidelberg, Germany, 2012.

Publisher's Note: MDPI stays neutral with regard to jurisdictional claims in published maps and institutional affiliations.



© 2020 by the authors. Licensee MDPI, Basel, Switzerland. This article is an open access article distributed under the terms and conditions of the Creative Commons Attribution (CC BY) license (<http://creativecommons.org/licenses/by/4.0/>).